Aeroacoustic Optimization of Installed Propeller Configurations with Scattering and Shielding Effects

Maks J. Groom*
Department of Mathematics, Massachusetts Institute of Technology
Simons Building, 77 Massachusetts Avenue, Cambridge, MA 02139

Beckett Y. Zhou†
Department of Aerospace Engineering, University of Bristol
Queens Building, University Walk, Bristol, BS8 1TR, United Kingdom

Leonard V. Lopes‡
Aeroacoustics Branch, NASA Langley Research Center
Hampton, VA 23681

An optimization capability is developed for acoustic scattering and shielding of installed propellers and rotors, based on a spacetime Galerkin time domain boundary element method (TDBEM). The time domain approach is particularly suitable for efficient simulation of transient, rotating, and broadband noise sources such as propellers. The use of algorithmic differentiation allows efficient evaluation of design sensitivities required for gradient-based design optimization with a large number of design variables. We present a validation exercise for the coherent broadband scattering capability against an analytical solution, showing excellent agreement. We then demonstrate the optimization tool on a series of inverse design cases with broadband and rotating sources, as well as an optimization problem for a propeller-wing configuration. The results show good performance for optimization problems with the characteristics of realistic installed propeller configurations.

I. Introduction

Recently, advanced air mobility (AAM) concepts have garnered significant interest from aircraft manufacturers, research institutions, academia, and government agencies. As cities grow, AAM systems can provide alternatives to increasingly congested transportation infrastructure. While many electric propeller-driven vertical takeoff and landing (eVTOL) concepts are currently under development for AAM applications that promise convenience and relative energy efficiency, noise pollution from aircraft in urban settings remains a major difficulty limiting widespread adoption of AAM systems and approval by regulators and community members.[1] In particular, the use of relatively quiet electric power systems in AAM configurations reduces engine noise and increases the relative significance of aerodynamic noise contributions in the overall noise footprint. It is, therefore, increasingly important to consider sources of noise as early as possible in the design process.

Design of AAM vehicles to achieve noise emission targets requires computationally efficient numerical tools that allow optimization of design parameters with acoustic objectives and constraints. Installed propellers constitute a particularly important noise source in many AAM configurations. Most previous studies that consider aeroacoustic optimization of propellers have focused on isolated configurations.[2–9] Pagano et al.[10] used semi-analytical approaches to include aerodynamic installation effects in their optimization, but acoustic installation effects such as scattering and shielding of propeller noise were not considered.

*Undergraduate Researcher; mgroom@mit.edu
†Lecturer in Aeroacoustics, AIAA Member; beckett.zhou@bristol.ac.uk
‡Senior Research Engineer, AIAA Member; leonard.v.lopes@nasa.gov.

Acoustic optimizations that include scattering and shielding effects have been performed, including for aircraft configurations,[11] scattering surface shape,[12] and acoustic liner characteristics.[13] However, these efforts have been limited to fixed point or harmonic mode approximations of acoustic sources, and do not generalize to propellers, which act as rotating acoustic source distributions with aperiodic broadband content. Scattering and shielding can be highly significant in installed propeller configurations,[14] motivating the development of new frameworks for aeroacoustic optimization that can address propeller acoustic installation effects.

Scattering methods for propeller and rotor noise, especially at early design stages, require specific source representations compared to other acoustic optimization problems. In particular, propellers are rotating, broadband noise sources, with significant low frequency content, which are difficult to represent with many conventional scattering techniques. Time domain boundary element methods are particularly suitable for propeller noise scattering because they can naturally model aperiodic, broadband signals with arbitrary source motion, and have good accuracy at low frequencies.

In this work, we develop a framework for gradient-based optimization of acoustic installation effects (scattering and shielding) in propeller-wing configurations using a spacetime Galerkin TDBEM approach.[15] This scattering method is selected to allow efficient representation of rotating propellers and aperiodic broadband sources, with maximum flexibility for single-layer and coincident source-scatterer surfaces. The remainder of this paper is organized as follows: Section II addresses the numerical schemes, including the Galerkin TDBEM and the gradient-based optimization framework; Section III presents validation results for scattering of coherent broadband sources; Section IV validates the optimization framework through a series of inverse design problems with broadband and rotating sources and an application to a propeller-wing scattering problem; finally, Section V draws some conclusions.

II. Methodology

II.A. Scattering Method

The scattering method obtains the total acoustic field as the sum of an incident component, which is the sound field due to the acoustic sources in the absence of scattering effects, and a scattered field, which is computed such that the total field satisfies the acoustic boundary condition on the scattering surface. With suitable assumptions on the mean background flow, variable transformations allow us to solve the scattering problem for the acoustic potential ϕ in the setting of the acoustic wave equation:

$$\frac{\partial^2 \phi}{\partial x_i^2} - \frac{1}{c_0^2}\frac{\partial^2 \phi}{\partial t} = s(\boldsymbol{x},t), \tag{1}$$

where s is an acoustic source distribution in the transformed coordinates, c_0 is the speed of sound, and x_i denote the Cartesian spatial coordinates in Einstein notation. Examples of these variable transformations include the Lorentz transformation (cf. Amiet and Sears[16]), the low Mach number approximation due to Taylor,[17] and the weakly nonuniform approximation of Mancini et al.,[18] which are appropriate for different types of mean flows.

This paper uses the sound-hard boundary condition, which is equivalent to requiring zero normal acoustic potential gradient. The solution to the scattering problem is obtained by solving (1) together with the boundary condition:

$$\frac{\partial \phi}{\partial n} = \frac{\partial \phi_i}{\partial n} + \frac{\partial \phi_s}{\partial n} = 0, \text{ on } \Gamma, \tag{2}$$

where the incident and scattered components are denoted with the subscripts ϕ_i and ϕ_s, $\frac{\partial}{\partial n}$ denotes the gradient in the normal direction, and Γ is the scattering surface.

The incident field is obtained by integrating the source distribution as:

$$\phi_i(\boldsymbol{x},t) = \int G(\boldsymbol{x},\boldsymbol{y},t,\tau) s(\boldsymbol{y},\tau) d\boldsymbol{y} d\tau, \tag{3}$$

where $\boldsymbol{x}$ and t are the observer space and time variables, $\boldsymbol{y}$ and τ are emission space and time variables, and $G(\boldsymbol{x},\boldsymbol{y},t,\tau)$ is the free-space Green's function for the acoustic wave equation:

$$G(\boldsymbol{x},\boldsymbol{y},t,\tau) = \frac{\delta\left(t-\tau-\frac{|\boldsymbol{x}-\boldsymbol{y}|}{c_0}\right)}{4\pi|\boldsymbol{x}-\boldsymbol{y}|}. \tag{4}$$

The normal gradient on the boundary is:

$$\frac{\partial \phi_i}{\partial n_{\boldsymbol{x}}}(\boldsymbol{x},t) = \int \frac{\partial G}{\partial n_{\boldsymbol{x}}} s(\boldsymbol{y},\tau) d\boldsymbol{y} d\tau = -g(\boldsymbol{x},t). \tag{5}$$

To obtain a total field that satisfies the boundary condition, the scattered field must be a homogeneous solution of (1) (i.e., with $s(\boldsymbol{x},t) = 0$) with the Neumann boundary condition:

$$\frac{\partial \phi_s}{\partial n_{\boldsymbol{x}}}(\boldsymbol{x},t) = g(\boldsymbol{x},t) \text{ on } \Gamma. \tag{6}$$

To compute the total acoustic field, we first compute the Neumann data g from the acoustic source distribution according to (5), as well as the incident field. Suitable methods include widely-used coupled CFD-computational aeroacoustics (CAA) methods, such as the Ffowcs Williams-Hawkings (FWH) aeroacoustic analogy,[19] which is often implemented according to the Formulation 1A of Farassat[20] for acoustic pressure and the corresponding G1A formulation of Lee et al.[21] for the pressure gradient. The incident field can also be specified with simple sources or semi-analytical propeller models, such as the model of Garrick and Watkins.[22] The method can therefore be coupled to both low-fidelity and high-fidelity input data depending on the application.

The TDBEM is then invoked to solve for the scattered field from the specified Neumann data. Our TDBEM[15] is based on the first kind spacetime-conforming Galerkin formulation of Ha-Duong.[23] The boundary element approach represents the scattered field with surface distributions of the double layer potential, which corresponds to the jump in acoustic potential over the boundary $\psi = \left[\frac{\partial \phi_s}{\partial n}\right]$. The first kind boundary integral equation for the double layer potential is:

$$g(\boldsymbol{x},t) = \frac{\partial \phi_s}{\partial n_{\boldsymbol{x}}}(\boldsymbol{x},t) = \int_0^t \int_\Gamma \frac{\partial^2 G}{\partial n_{\boldsymbol{x}} \partial n_{\boldsymbol{y}}} \psi(\boldsymbol{y}, \tau - |\boldsymbol{x}-\boldsymbol{y}|) d\boldsymbol{y} d\tau, \tag{7}$$

for $\boldsymbol{x} \in \Gamma$, $t \in [0,T]$. Bamberger and Ha-Duong[24] show that the appropriate weak form of (7) for full Galerkin discretization is:

$$a(\psi,\eta) := \int_0^T \int_\Gamma \dot{\eta}(\boldsymbol{x},t) \int_\Gamma \frac{\partial^2 G}{\partial n_{\boldsymbol{x}} \partial n_{\boldsymbol{y}}} \psi(\boldsymbol{y}, t - |\boldsymbol{x}-\boldsymbol{y}|) d\boldsymbol{y} d\boldsymbol{x} dt = f(\eta) := \int_0^T \int_\Gamma \dot{\eta}(\boldsymbol{x},t) g(\boldsymbol{x},t) d\boldsymbol{x} dt, \tag{8}$$

for all test functions η belonging to the same space as the trial functions, where $\dot{\eta}$ denotes the time derivative.

The weak form is discretized with piecewise linear test and trial basis elements in space and time on a triangular surface mesh. While the spatial and temporal resolutions are not limited by stability requirements, the ratio of spatial and temporal steps must be chosen to satisfy causality. The condition is:

$$\text{CFL} = \frac{c_0 \Delta t}{\Delta x} \leq 1. \tag{9}$$

In practice, we have found that a value of $\text{CFL} = 0.8$ performs well.[15]

The spacetime Galerkin formulation is notable for being unconditionally stable.[23,24] It also has a number of numerical and practical advantages over alternative TDBEM schemes, such as Burton-Miller reformulation with point collocation.[25] Galerkin approaches avoid the introduction of additional numerical parameters that must be tuned, as is the case in Burton-Miller reformulation, where a coupling parameter must be chosen carefully to obtain accurate results.[26] The double spatial integration required by the full Galerkin approach gives greater flexibility because it allows simulation of open scattering surfaces and coincident source-scatterer surfaces, which result in hypersingular integrands in the collocation approach. Finally, Galerkin methods benefit from a quasi-best approximation property in the energy norm that tends to result in more accurate solutions with a given discretization compared to collocation methods,[27] which may be particularly beneficial given the high asymptotic cost scaling of integral methods.

II.B. Optimization Framework

From the scattering model, a design tool is developed to perform gradient-based optimization with acoustic constraints or objectives. The design variables can be vehicle or configuration geometry parameters, which currently included the orientation and position of scattering bodies and noise sources, as well as noise source properties. The noise generated by the configuration, including scattering effects, can be included as a constraint or objective through noise metrics computed from the pressure signals at the user-defined observer locations. The derivatives of the constraints or objectives with respect to the design variables are obtained by algorithmic differentiation of the implementation in reverse (adjoint) mode. This approach allows efficient evaluation of sensitivities of a large number of design variables. The derivatives are then passed to a gradient-based optimization scheme to obtain a solution to the optimization problem.

The TDBEM described in Section II.A takes the gradient of the incident acoustic field on the scattering surface as an input to obtain the boundary data. Additionally, the incident field must be added to the scattered field obtained with the TDBEM in order to compute the total farfield noise. If the incident field solution depends on the design variables, its sensitivities with respect to the design variables must also be computed. As the goal of this paper is to emphasize the acoustic scattering methodology rather than the aeroacoustic methodology for the incident field, we consider optimization problems in which the propeller/acoustic source is specified independently from the design variables being optimized. Therefore, the sensitivities of the source distribution to the design variables will be zero, and we focus on obtaining and validating design sensitivities for the acoustic solver.

The scattering method and all other components of the acoustic analysis (evaluation of the incident field and any variable transformations to account for mean flow) are implemented in Python using the JAX framework.[28] JAX has a built-in automatic differentiation capability, and also uses XLA (Accelerated Linear Algebra) compilation to run the code efficiently on GPUs. The optimization problem is solved with the box-constrained limited-memory Broyden–Fletcher–Goldfarb–Shanno (L-BFGS-B) algorithm implemented in JAXopt,[29] a Python optimization package developed to interface with JAX. The L-BFGS-B method is well suited to optimization problems with a high number of design variables with box constraints. All design variables (currently source position and orientation coordinates) are normalized to take values bounded between zero and one to ensure that extreme parameter magnitudes do not dominate the gradients. The acoustic variables are used to construct constraint and objective functions that are similarly normalized to one at the initial guess.

III. Validation for Broadband Sources

The scattering method was previously validated for harmonic point sources in several test cases with available analytical results, as well as for rotating sources via a comparison with experimental results for a propeller near a flat plate.[15] To establish the performance of the scattering method for broadband signals, we consider a validation case consisting of a broadband point source over a unit sphere. The source is placed at a radius of $r_s = 2$, with observers located in a circular array centered on the source point with a radius of $r_o = 5$ in a plane that contains the center of the sphere (see Figure 1). The computations were performed on a fixed-resolution mesh with 1280 faces and 642 nodes, with $c_0 = 1$. To compare with steady-state reference solutions, the simulations are all run until initial transients have left the domain before data are collected.

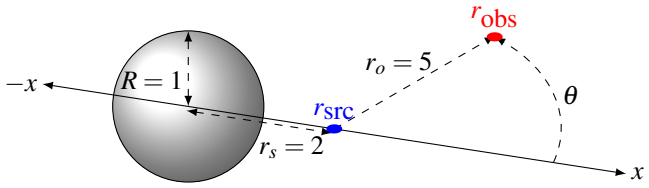

Figure 1: Diagram of sphere geometry showing the source (blue dot, $\boldsymbol{r}_{\text{src}}$) and observer (red dot, $\boldsymbol{r}_{\text{obs}}$) coordinates.

A coherent broadband signal for the point source is constructed by specifying the desired spectrum in the frequency domain. Based on the fixed temporal timestep, the spectrum is discretized at discrete Fourier transform sample frequencies ω to obtain Fourier series coefficients, which then receive a random phase shift. The incident field for the point source located at $\boldsymbol{r}_{src}$ is then evaluated as:

$$p_i(\boldsymbol{x},t) = \frac{f(t-|\boldsymbol{x}-\boldsymbol{r}_{src}|)}{4\pi|\boldsymbol{x}-\boldsymbol{r}_{src}|}, \tag{10}$$

where $f(t)$ is the Fourier series in the time domain. To construct the analytical solution, the exact steady-state harmonic solution provided by Bowman et al.[30] is evaluated at each of the discrete sample frequencies, and multiplied by the corresponding Fourier coefficient.

We first consider a broadband source with a uniform unit spectrum between wavenumbers $k_{min} = \omega_{min}/c_0 = 1$ and $k_{max} = \omega_{max}/c_0 = 5$. Figure 2 compares the numerical and exact spectra of the total acoustic field at selected observer locations. All angles and frequencies show very strong alignment between the numerical and analytical solutions, with slight deviations visible at higher wavenumbers for $\theta = 90°$.

Next, we compare the overall directivity by plotting the root mean square (RMS) of the acoustic pressure components in Figure 3a. We see very strong agreement between the numerical and exact solutions, which are essentially indistinguishable. We also consider a narrower broadband spectrum that is uniform between wavenumbers $k_{min} = 5$

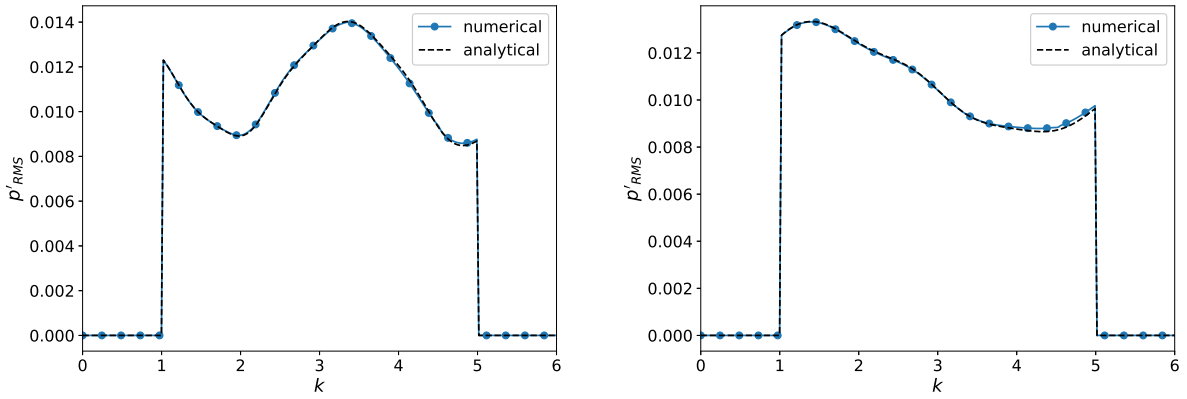

(a) $\theta = 0°$

(b) $\theta = 90°$

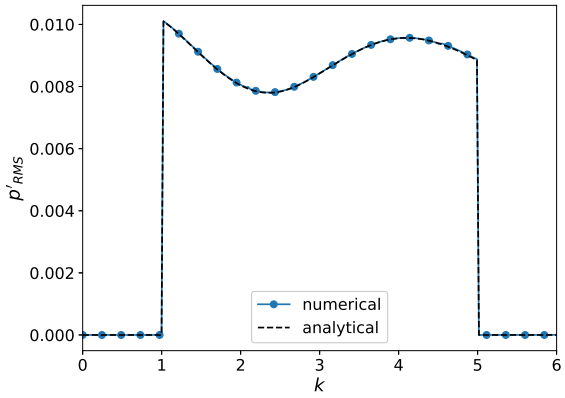

(c) $\theta = 150°$

Figure 2: Pressure spectra for the sphere scattering case forced with a uniform broadband signal from $k = 1$ to $k = 5$ at selected observer angles. The numerical solution (solid blue line) aligns closely with the analytical solution (dashed black line) at all angles and frequencies.

and $k_{max} = 6$ (Figure 3b). The alignment between numerical and exact solutions is similarly strong. The combination of a narrower bandwidth and higher average frequency results in a more prominently lobed directivity.

Finally, we use the broadband source test case to assess the resolution requirements of the scattering method. For frequencies corresponding to wavelengths less than twice the spatial node spacing (Nyquist sampling limit), the discretization results in information loss due to aliasing. With the selected mesh resolution, the maximum wavenumber before aliasing occurs is $k_{lim} = 19.08$. Using a very wide broadband signal that is uniform between wavenumbers $k_{min} = 1$ and $k_{max} = 30$, we can assess the performance of the scattering method as it approaches and exceeds this wavenumber limit.

Figure 4 shows two different plots of the p'_{RMS} spectrum at the $\theta = 0°$ observer location. The figures show reasonable results below around $k = 10$, or 4 points per wavelength, defined as the ratio of the wavelength to the maximum element edge length (the sampling limit corresponds to 2 points per wavelength). Closer to the wavenumber limit, the signal is very poorly resolved. Above the limit, the signal bears minimal relation to the analytical solution, as is expected. This result suggests an initial recommendation of 4 points per wavelength, at least for smooth scattering surfaces, to ensure adequate resolution of a particular wavenumber.

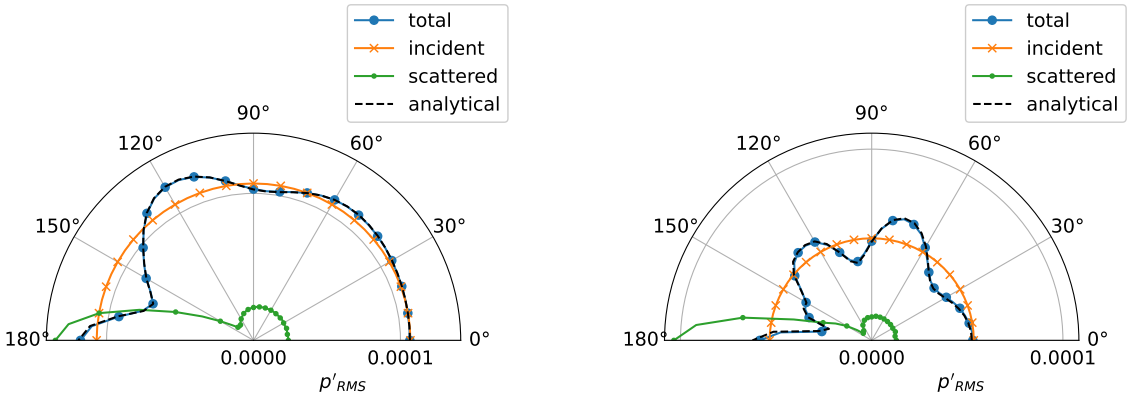

(a) Uniform broadband from $k = 1$ to $k = 5$.

(b) Uniform broadband from $k = 5$ to $k = 6$.

Figure 3: Polar plots of RMS acoustic pressure p'_{RMS} for the broadband sphere case, comparing the incident (orange solid line), scattered (green solid line), and total (blue solid line) numerical fields with the analytical solution (black dashed line). (a) Forcing with a uniform broadband signal from $k = 1$ to $k = 5$. (b) Forcing with a uniform broadband signal from $k = 5$ to $k = 6$.

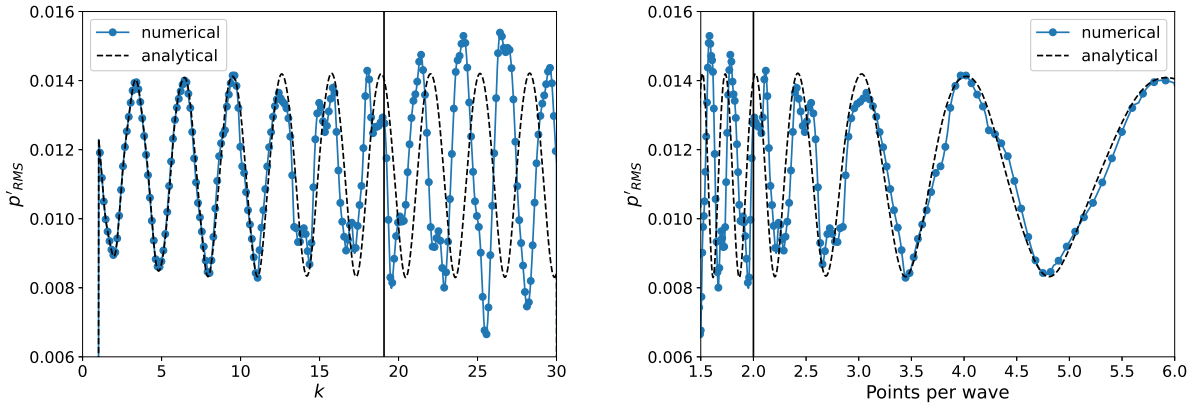

(a) p'_{RMS} spectrum plotted against wavenumber k.

(b) p'_{RMS} spectrum plotted against spatial points per wavelength.

Figure 4: Pressure spectra at $\theta = 0$ for a uniform broadband signal from $k = 1$ to $k = 30$, showing the effect of resolution on numerical accuracy. (a) Pressure spectrum plotted against wavenumber. The vertical black line marks the frequency corresponding to the spatial sampling limit. (b) Pressure spectrum plotted against the ratio of the wavelength to the maximum element edge length.

IV. Optimization Results

IV.A. Inverse Design

To test our optimization capability, we first consider some simple inverse design cases. The configurations are very loosely inspired by multi-rotor AAM configurations in hover. The geometries consist of a unit sphere as a scatterer, with pairs of sources at mirrored locations on either side of a centerplane through the scattering body, as illustrated in Figure 5. This results in three design parameters per source pair: a vertical coordinate z, measured from the center of the sphere, a radial coordinate in the plane orthogonal to the z axis, also measured from the center of the sphere, and a polar angle θ, measured from the centerplane. The idea of the inverse design is to recover a set of predetermined target source configuration design variables from a randomly perturbed initial set of design variables, using the optimization framework with an acoustic objective function.

Table 1: Initial and target normalized design parameter values for the inverse design problems. The normalized coordinates for each source pair are listed in rows in the order r, θ, z. The initial configurations are randomly generated, while the target configurations are chosen as the midpoint of the parameter space.

Number of source pairs	Initial configuration (r, θ, z)	Target configuration (r, θ, z)
1	0.29845604, 0.73010999, 0.91640042	0.5, 0.5, 0.5
2	0.08150064, 0.26759223, 0.49447796	0.5, 0.5, 0.5
	0.52517907, 0.06121185, 0.86910146	0.5, 0.5, 0.5
3	0.15641490 , 0.64139559, 0.80261572	0.5, 0.5, 0.5
	0.50561505, 0.33932627, 0.22153479	0.5, 0.5, 0.5
	0.23964215, 0.74317318, 0.06322572	0.5, 0.5, 0.5

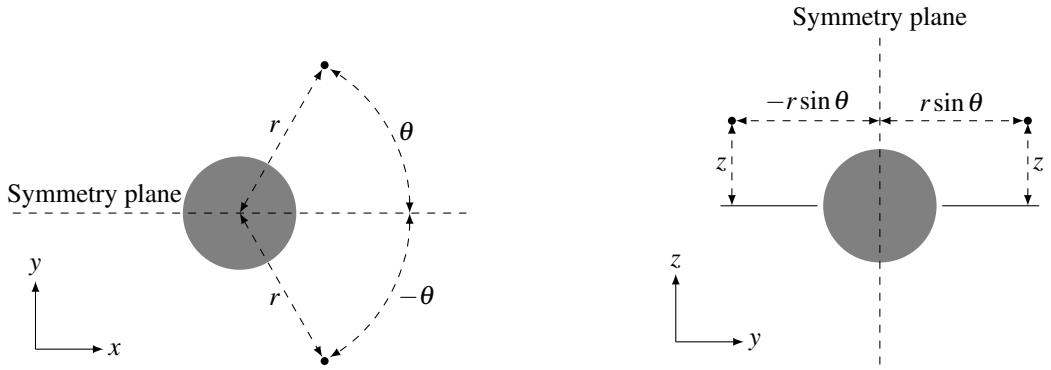

(a) xy plane. (b) yz plane.

Figure 5: Diagram of the inverse design setup showing the design parameters (r, θ, z) that define the locations of a mirrored source pair in cylindrical coordinates.

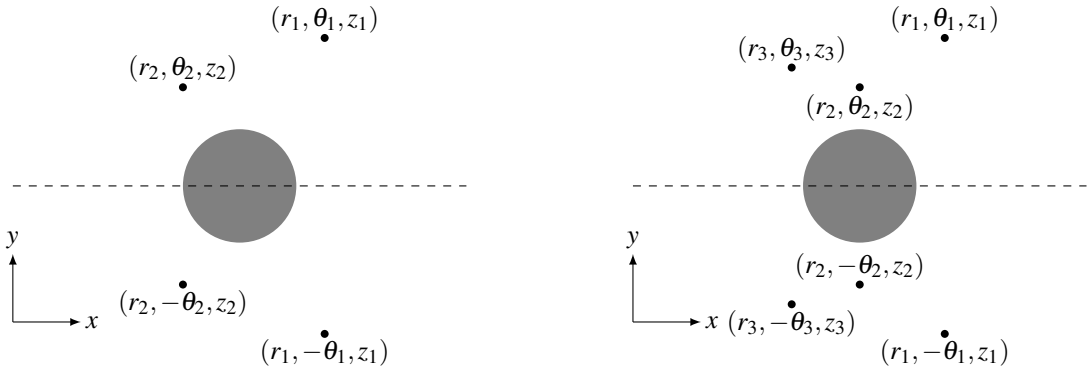

(a) 2 source pairs. (b) 3 source pairs.

Figure 6: Diagrams of the inverse design setup for 2 and 3 pairs in the xy plane.

The objective is constructed by considering an observer hemisphere with a radius of 5, centered directly below the scatterer. The hemisphere has 19 even angular divisions in both the polar and azimuthal directions, resulting in 325 unique observer locations. The polar axis is aligned with the centerplane of the scattering body, which is also the symmetry plane of the source configuration. The objective consists of the squared L^2 norm of the difference between the current p'_{RMS} values at the observer points and the p'_{RMS} values at the observers when the sources are in the predetermined target configuration. The objective is normalized by its initial value to range between one at the initial condition and zero at the target configuration, and is quadratic around the optimum by construction.

Inverse design problems were considered with one, two, and three pairs of sources. For all source pairs in all three cases, the radial coordinates take values in the interval $[2,3]$, while the vertical coordinates take values in the interval $[0.5,2]$. For one source pair, $\theta \in [0^\circ, 180^\circ]$; for two source pairs, $\theta_1 \in [10^\circ, 80^\circ]$ and $\theta_2 \in [100^\circ, 170^\circ]$; for three source pairs, $\theta_1 \in [15^\circ, 45^\circ]$, $\theta_2 \in [75^\circ, 105^\circ]$, and $\theta_3 \in [135^\circ, 165^\circ]$. As previously outlined, these design variables are mapped to optimization parameters that are normalized to take values between zero and one.

For each inverse design problem, the target configuration is selected as the midpoint of the parameter space, which corresponds to 0.5 for each normalized value of the radial, angular, and vertical coordinates of each source pair. The problems are initialized from randomly generated initial configurations, which are summarized in Table 1. The solutions are converged to a tolerance of 10^{-10}. Each inverse design case is performed twice, once with broadband point sources, and once with rotating sources.

IV.A.1. Inverse Problem with Broadband Sources

The broadband inverse design problem used two independently realized coherent broadband signals for each mirrored pair of source points, with uniform spectra between $k_{min} = 1$ and $k_{max} = 5$. To avoid contaminating the sensitivities, the signals were randomly generated at the beginning of the optimization, but stored between successive iterations.

The broadband inverse design results are summarized in Table 2, showing convergence to within 10^{-6} of the target configurations in all design parameters within 25 iterations. The convergence of the objective function and the gradient for each case are shown in Figure 7. The Frobenius norm, normalized by the gradient at the first iteration, is used to assess the gradient convergence. Both the objective and the gradient converge rapidly and towards the optimum, and are reduced by at least 12 and 6 orders of magnitude, respectively.

Table 2: Inverse design results with broadband point sources. The optimized configurations are reported as normalized values.

Source pairs	Iterations	Optimized configuration (r, θ, z)
1	16	0.50000022, 0.50000005, 0.50000061
2	21	0.49999951, 0.50000006, 0.50000029
		0.50000010, 0.50000005, 0.50000008
3	22	0.49999991, 0.50000009, 0.49999990
		0.50000003, 0.50000000, 0.49999998
		0.50000015, 0.49999994, 0.49999996

For illustration purposes, the directivities on the observer hemispheres are compared for the initial, target, and optimized configurations in the three broadband source pair case in Figure 8. The target and optimized directivities are essentially coincident, with a maximum pointwise p'_{RMS} difference on the order of 10^{-10}.

IV.A.2. Inverse Problem with Rotating Sources

The inverse design case is also performed using the Garrick-Watkins semi-analytical propeller model.[22] The propellers are oriented along the vertical axis and centered on the specified source points. The blade passing frequency is set to correspond to the wavenumber $k = 2$. The mirrored propellers in each pair are counter-rotating and phase locked. Other parameters, such as the thrust and torque values, are summarized for each case in Table 3. Many of these parameters could be explored as design variables in future optimization problems.

The Garrick-Watkins propeller inverse design results are summarized in Table 4, showing convergence to within 10^{-5} of the target configurations in all design parameters within 25 iterations. The convergence of the objective function and the gradient for each case are shown in Figure 9. The gradient convergence is again measured by the Frobenius norm, normalized by the gradient at the first iteration. Both the objective and the gradient converge rapidly and towards the optimum, and are reduced by at least 9 and 5 orders of magnitude, respectively.

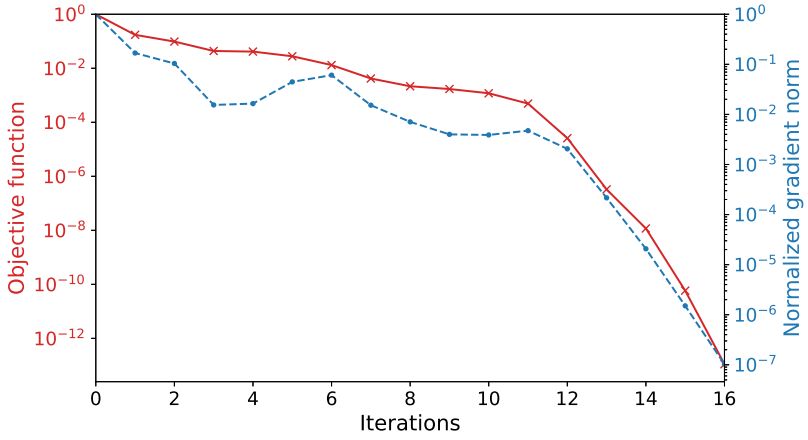

(a) One source pair.

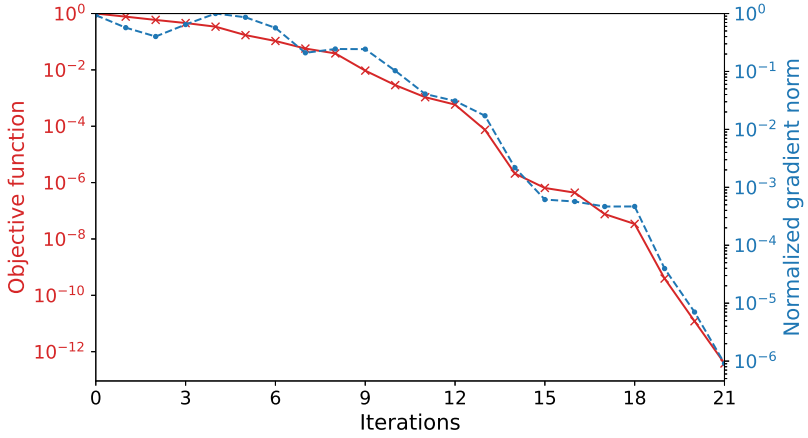

(b) Two source pairs.

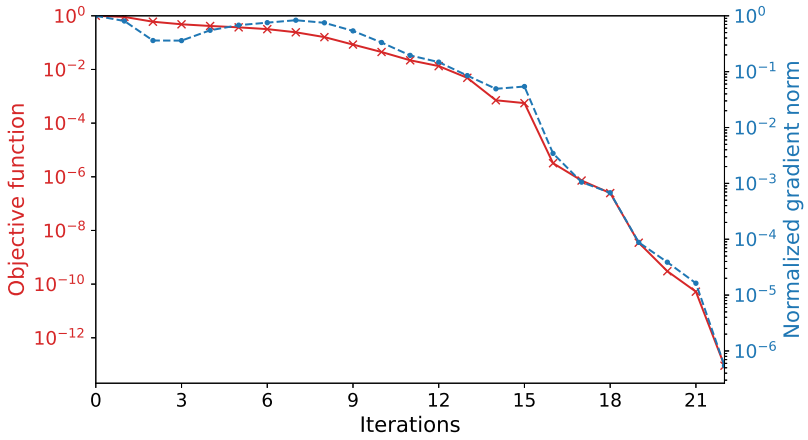

(c) Three source pairs.

Figure 7: Convergence plots showing rapid reduction of the objective function and the normalized gradient norm (Frobenius norm, normalized by the first iteration) for the inverse design cases with broadband point sources.

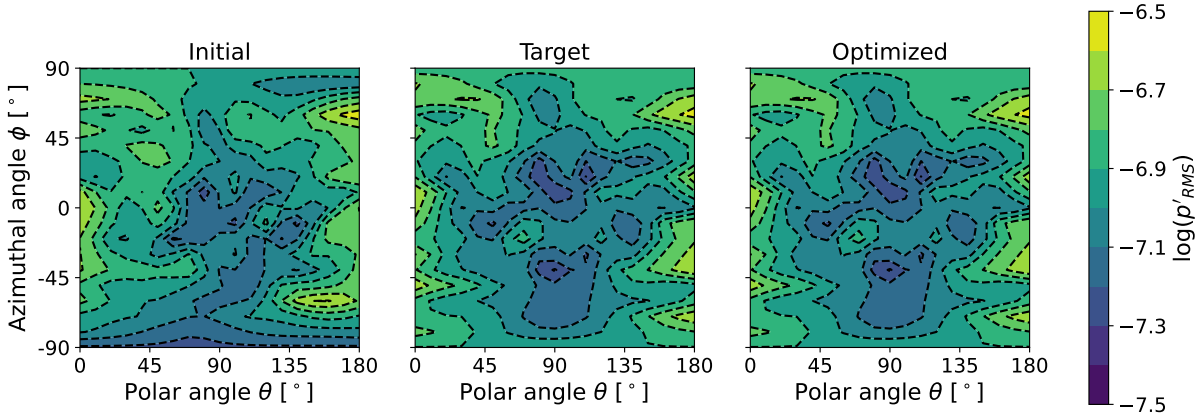

Figure 8: Comparison of the $\log(p'_{RMS})$ footprints on the observer hemisphere for the target, initial, and optimized source configurations for the three source pair broadband inverse design problem.

Table 3: Parameters for the Garrick-Watkins propeller model used in the inverse design problems.

Source pairs	Number of blades	Blade length	Thrust T	Torque Q
1	3	1	4	0.1
2	2	0.75	2	0.05
3	2	0.5	1.33	0.033

Table 4: Inverse design results with rotating sources. The optimized configurations are reported as normalized values.

Source pairs	Iterations	Optimized configuration (r, θ, z)
1	17	0.49999999, 0.50000000, 0.50000001
2	15	0.50000707, 0.49999952, 0.49999292
		0.49999038, 0.50000080 , 0.49999749
3	24	0.50000137, 0.50000047, 0.50000137
		0.50000021, 0.49999853, 0.50000086
		0.49999785, 0.49999875, 0.50000114

Figure 10 compares the directivities on the observer hemispheres for the initial, target, and optimized configurations in the three source pair Garrick-Watkins case. The target and optimized directivities are essentially coincident, with a maximum pointwise p'_{RMS} difference on the order of 10^{-8}.

IV.B. Optimization of a Propeller-Wing Configuration

We now perform an optimization for a simple configuration with two lifting propellers positioned below the leading edge of a wing in hover. The wing is represented by a single-layer flat plate, with a unit span and a chord of 0.3, discretized with 648 panels. The sources consist of two Garrick-Watkins propellers, oriented along the vertical axis, with opposite rotations at mirrored locations on either side of the wing centerline, as shown in Figure 11. The origin of the Cartesian coordinates is defined as the leading edge of the wing at the symmetry plane, and the source position parameters take values in the intervals $x \in [0.2, 0.5]$, $y \in [0.25, 0.75]$, and $z \in [0.25, 0.75]$. As in the inverse design problems, the parameters are mapped to normalized design variables that take values between zero and one. The Garrick-Watkins propellers each have three blades, with a diameter of 0.5, and a blade passing frequency corresponding to the wavenumber $k = 5$. The mirrored propellers are counter-rotating and phase-locked. The thrust and torque for each propeller are $T = 1$ and $Q = 0.025$, respectively. As with the inverse design problems, aerodynamic installation effects on the propellers or the wing are not included.

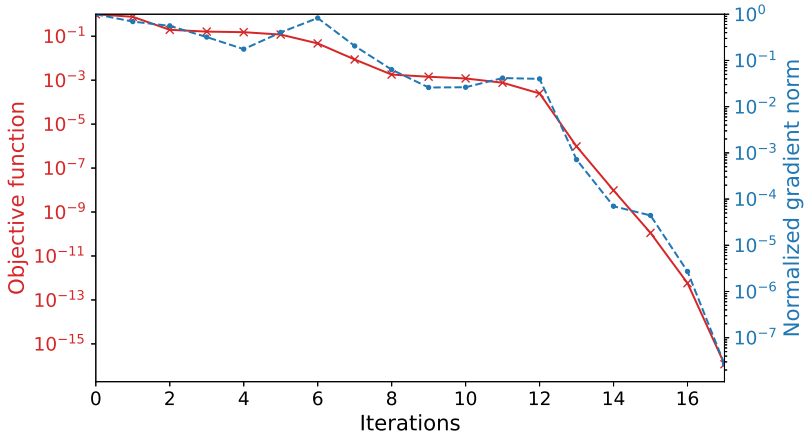

(a) One source pair.

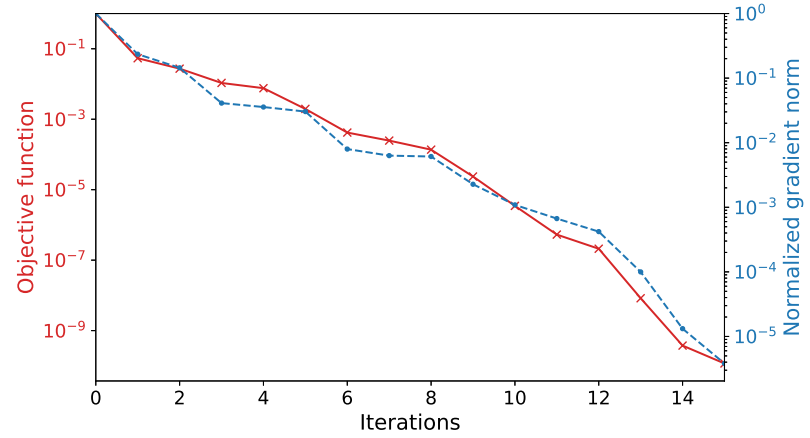

(b) Two source pairs.

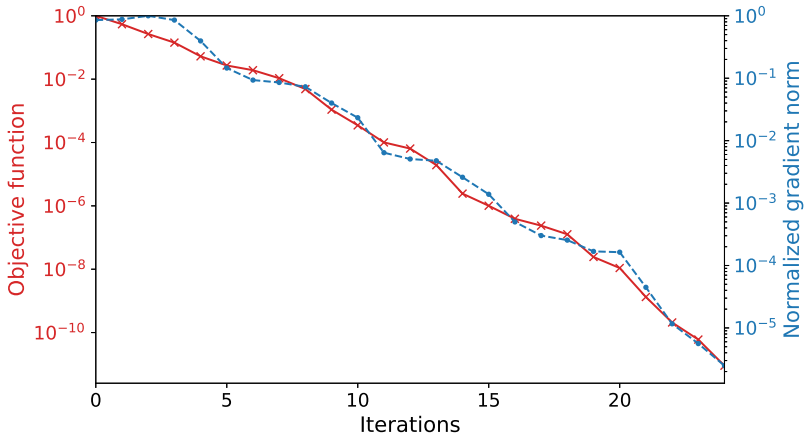

(c) Three source pairs.

Figure 9: Convergence plots showing rapid reduction of the objective function and the normalized gradient norm (Frobenius norm, normalized by the first iteration) for the inverse design cases with rotating sources.

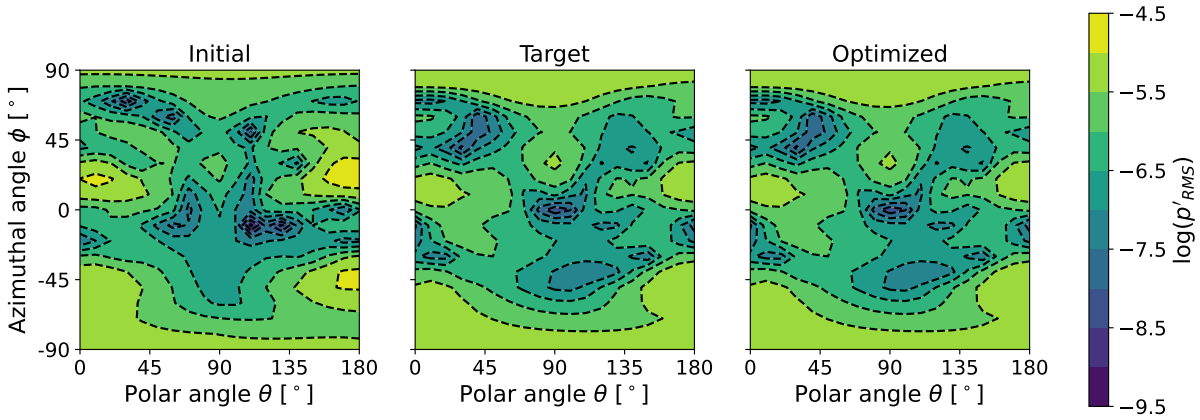

Figure 10: Comparison of the $\log(p'_{RMS})$ footprints on the observer hemisphere for the target, initial, and optimized source configurations for the three source pair Garrick-Watkins inverse design problem.

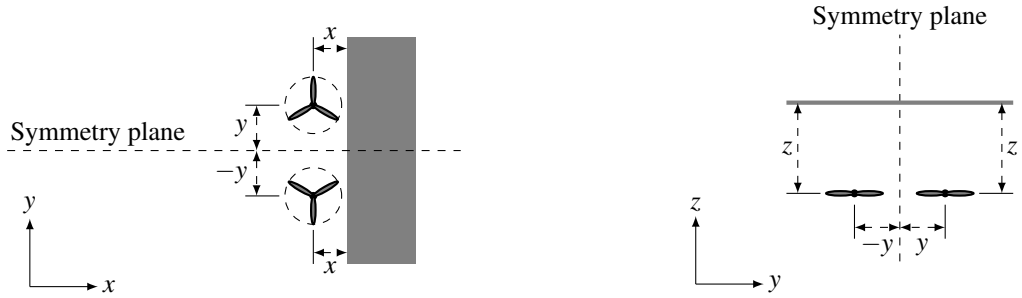

(a) xy plane.

(b) yz plane.

Figure 11: Diagram of the optimization case setup showing the design parameters (x, y, z) that define the locations of a mirrored pair of propellers relative to the wing leading edge.

The same observer hemisphere with a radius of 5 and 325 unique observer locations is used, centered on the leading edge of the wing at the symmetry plane. The objective is defined as the squared L^2 norm of the p'_{RMS} values at the observer points, and is normalized by its initial value. The optimization was performed starting from an initial location at the midpoint of the parameter space (all normalized parameters equal to 0.5, corresponding to $x = 0.35$, $y = \pm 0.5$, and $z = 0.5$), both with and without the scattered contribution. The distance from the center of the propellers in the initial configuration to the center of the hemisphere at the origin is around 0.789.

Figure 12 shows the reduction of the objective and gradient norm for the optimization case run both with and without the scattering contribution. Both cases see approximately 7.7% improvements in the objective after 13 and 11 iterations, respectively. The gradient is also reduced but does not vanish because the optimized solutions are on the boundary of the design space.

Table 5: Comparison of optimized results with and without the scattering contribution, reported as normalized values.

Case	Iterations	Optimized configuration (x, y, z)
Total	13	1.00000000, 0.90483659, 0.00000000
Incident only	11	0.00000000, 0.89510975, 0.00000000

While the improvements are similar, the inclusion or exclusion of the scattering contribution results in different optimized solutions, which are summarized in Table 5. In both cases, the optimizer pushes the last coordinate, which corresponds to the vertical separation of the propellers below the wing, to the lower bound. By lifting the propellers in this way, the optimizer moves them farther from the observer locations. In the first coordinate, which corresponds

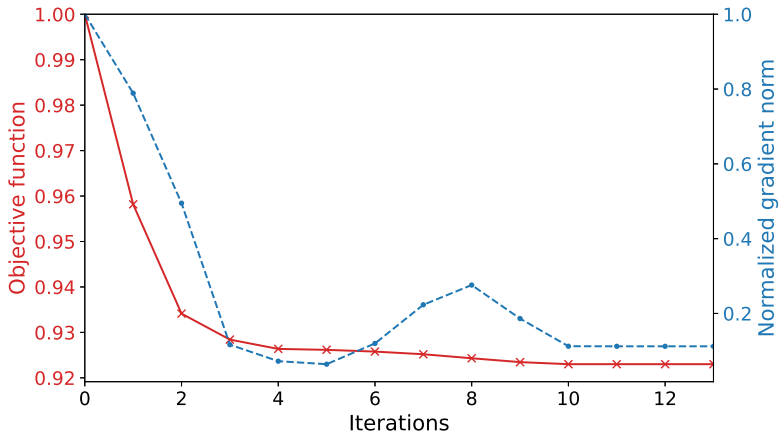

(a) Total (incident and scattered contributions).

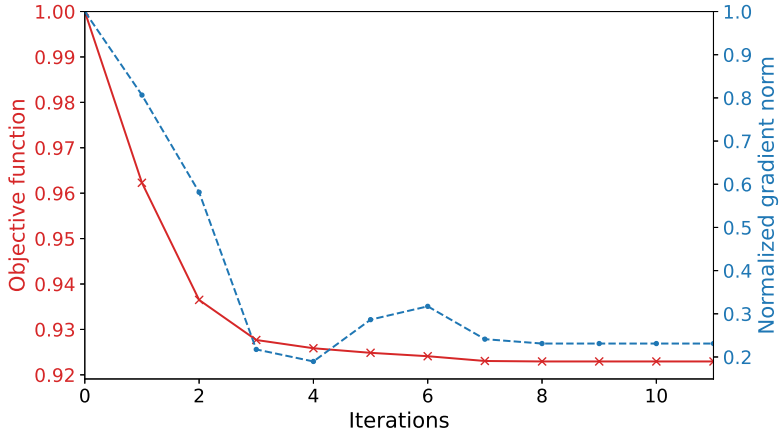

(b) Incident contribution only.

Figure 12: Convergence plots showing reduction of the objective function and the normalized gradient norm (Frobenius norm, normalized by the first iteration) for the optimization problem both with (top) and without (bottom) the scattering contribution.

to the chordwise separation of the propellers from the leading edge of the wing, the behavior is qualitatively different. Without scattering effects, the optimizer again pushes the propeller locations to the lower bound, as far from the observers as possible. When the scattering effects are included, the optimizer pushes the propeller locations to the opposite bound, maximizing separation from the wing at the cost of moving closer to the observers in order to minimize the noise contribution from the acoustic interaction with the wing. The optimized solutions for the middle coordinate, corresponding to the spanwise separation between the propellers, are similar for the two cases, converging to similar values between the bounds. The spanwise separation increases compared to the initial configuration, possibly due to destructive interference between the acoustic fields of the two propellers. Overall, the distance from the propellers to the center of the hemispheres is slightly decreased without scattering effects to 0.768, while the distance is increased to 0.898 when scattering effects are included. The directivities on the observer hemispheres are compared for the initial and optimized configurations, with and without scattering contributions, in Figure 13. The optimized solution with scattering effects shows noticeably higher noise at negative azimuthal angles due to the increased horizontal separation from the wing leading edge.

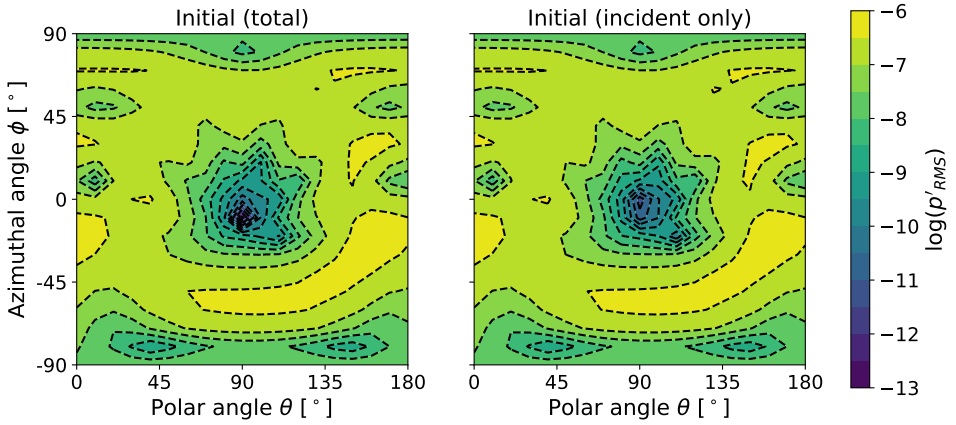

(a) Noise footprints for the initial configuration.

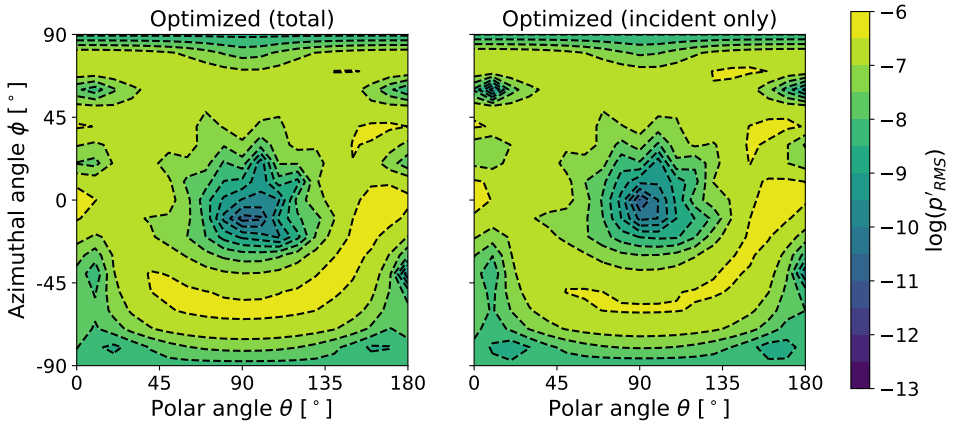

(b) Noise footprints for the optimized configurations.

Figure 13: Comparison of the $\log(p'_{RMS})$ footprints on the observer hemisphere for the (a) initial and (b) optimized propeller configurations obtained with and without scattering effects.

V. Conclusions and Future Work

In this work, we present a method for optimization of installed propeller configurations with scattering and shielding effects. The rotating, broadband character of propeller noise sources motivates the use of a recently developed Galerkin TDBEM scattering model,[15] which is presently extended to obtain design sensitivities. Sensitivities are obtained by algorithmic differentiation through JAX, which allows for efficient and robust evaluation for large numbers of design variables. The spacetime Galerkin approach offers a robust, flexible, and efficient scattering method that is well-suited to both high-fidelity and mid-fidelity design and prediction problems. The TDBEM implementation can be integrated with any CFD-CAA method that can provide the incident acoustic field and its gradient.

Continuing the previous validation campaign, we present a validation case for a broadband source scattered by a sphere, demonstrating very good alignment at all angles and frequencies, and for both wide and narrow bandwidths. The broadband case is used to evaluate the spatial resolution requirements, resulting in a recommendation of a minimum of roughly 4 spatial points per wavelength of the highest resolved frequency.

Next, we provide an initial demonstration of the optimization capability, applying the optimization tool to a series of inverse design problems for the location of source points positioned around a scattering body. The inverse design problems were each performed twice, with broadband point sources and Garrick-Watkins propellers respectively, demonstrating excellent results with both broadband and rotating sources.

Finally, we consider an optimization problem consisting of two lifting propellers placed in front of and below the leading edge of a wing. Optimizations are performed with and without the scattering contribution, converging to qualitatively different solutions due to the presence or absence of the scatterer. This behavior emphasizes the importance of including scattering effects in acoustic optimizations of installed propeller configurations.

Overall, the present method appears to have strong potential for computationally efficient optimization of propeller and rotor noise scattering. Further work will include an application of the scattering capability to a multidisciplinary optimization problem, as well as the demonstration of additional capabilities within the scattering tool, including the effects of nonzero mean background flows, full tool chain integration with sensitivities of the incident field, and deformation of the scattering surfaces.

VI. Acknowledgments

The first author gratefully acknowledges support from the NASA Langley Research Center, as well as funding from the MIT Undergraduate Research Opportunities Program, including the Paul E. Gray (1954) UROP Fund.

References

[1]Vascik, P. D., Hansman, R. J., and Dunn, N. S., "Analysis of urban air mobility operational constraints," *Journal of Air Transportation*, Vol. 26, No. 4, 2018, pp. 133–146.

[2]Lopes, L. V. and Ingraham, D. J., "Influence of the perception constraint, observer position, and broadband self-noise on low-fidelity UAM vehicle perception-influenced-design (PID) optimization," *Vertical Flight Society's 79th Annual Forum & Technology Display*, 2023.

[3]Abergo, L., Morelli, M., Pullin, S. F., Zhou, B. Y., and Guardone, A., "Adjoint-based aeroacoustic optimization of propeller blades in rotating reference frame," *AIAA Aviation 2023 Forum*, AIAA Paper 2023-3836.

[4]Pullin, S. F., Zhou, B. Y., and Azarpeyvand, M., "Optimisation of propellers with noise-based constraints including a deep learning method for aerofoil prediction," *28th AIAA/CEAS Aeroacoustics 2022 Conference*, AIAA Paper 2022-3073.

[5]Li Volsi, P., Gomez-Ariza, D., Gojon, R., Jardin, T., and Moschetta, J.-M., "Aeroacoustic optimization of MAV rotors," *International Journal of Micro Air Vehicles*, Vol. 14, 2022.

[6]Kümmel, A., Stuhlpfarrer, M., Pölzlbauer, P., and Breitsamter, C., "Propeller blade shape optimization with a hybrid BEMT/CFD approach," *New Results in Numerical and Experimental Fluid Mechanics XII: Contributions to the 21st STAB/DGLR Symposium, Darmstadt, Germany, 2018*, Springer, 2020, pp. 362–371.

[7]Ingraham, D., Gray, J. S., and Lopes, L. V., "Gradient-based propeller optimization with acoustic constraints," *AIAA SCITECH 2019 Forum*, AIAA Paper 2019-1219.

[8]Gur, O. and Rosen, A., "Optimization of propeller based propulsion system," *Journal of Aircraft*, Vol. 46, No. 1, 2009, pp. 95–106.

[9]Miller, C. J. and Sullivan, J. P., "Noise constraints effecting optimal propeller designs," *SAE transactions*, Vol. 94, 1985, pp. 585–593.

[10]Pagano, A., Barbarino, M., Casalino, D., and Federico, L., "Tonal and broadband noise calculations for aeroacoustic optimization of a pusher propeller," *Journal of Aircraft*, Vol. 47, No. 3, 2010, pp. 835–848.

[11]Bryson, D. E., Marks, C. R., Miller, R. M., and Rumpfkeil, M. P., "Multidisciplinary design optimization of quiet, hybrid-electric small unmanned aerial systems," *Journal of Aircraft*, Vol. 53, No. 6, 2016, pp. 1958–1962.

[12]Divo, E., Kassab, A., and Ingber, M., "Shape optimization of acoustic scattering bodies," *Engineering Analysis with Boundary Elements*, Vol. 27, No. 7, 2003, pp. 695–703.

[13]Reimann, C., Tinetti, A., and Dunn, M., "Engine liner optimization using the fast scattering code," *13th AIAA/CEAS Aeroacoustics Conference (28th AIAA Aeroacoustics Conference)*, AIAA Paper 2007-3494.

[14]Zawodny, N. S., Boyd, D. D., and Nark, D. M., "Aerodynamic and acoustic interactions associated with inboard propeller-wing configurations," *AIAA Scitech 2021 Forum*, AIAA Paper 2021-0714.

[15]Groom, M. J., Pullin, S. F., Zhou, B., and Wang, Q., "A Galerkin time domain boundary element method for scattering and shielding of installed propeller noise," *AIAA SCITECH 2024 Forum*, AIAA Paper 2024-2810.

[16]Amiet, R. and Sears, W., "The aerodynamic noise of small-perturbation subsonic flows," *Journal of Fluid Mechanics*, Vol. 44, No. 2, 1970, pp. 227–235.

[17]Taylor, K., "A transformation of the acoustic equation with implications for wind-tunnel and low-speed flight tests," *Proceedings of the Royal Society of London. A. Mathematical and Physical Sciences*, Vol. 363, No. 1713, 1978, pp. 271–281.

[18]Mancini, S., Astley, R. J., Sinayoko, S., Gabard, G., and Tournour, M., "An integral formulation for wave propagation on weakly non-uniform potential flows," *Journal of Sound and Vibration*, Vol. 385, 2016, pp. 184–201.

[19]Ffowcs Williams, J. E. and Hawkings, D. L., "Sound generation by turbulence and surfaces in arbitrary motion," *Philosophical Transactions of the Royal Society of London. Series A, Mathematical and Physical Sciences*, Vol. 264, No. 1151, 1969, pp. 321–342.

[20]Farassat, F., "Derivation of formulations 1 and 1A of Farassat," *NASA/TM-2007-214853. NASA Langley Research Center*, 2007.

[21]Lee, S., Brentner, K. S., Farassat, F., and Morris, P. J., "Analytic formulation and numerical implementation of an acoustic pressure gradient prediction," *Journal of Sound and Vibration*, Vol. 319, No. 3-5, 2009, pp. 1200–1221.

[22]Garrick, I. and Watkins, C. E., "A theoretical study of the effect of forward speed on the free-space sound-pressure field around propellers," NACA TN 3018, 1953.

[23]Ha-Duong, T., "On retarded potential boundary integral equations and their discretisation," *Topics in Computational Wave Propagation: Direct and Inverse Problems*, 2003, pp. 301–336.

[24]Bamberger, A. and Duong, T. H., "Formulation variationnelle pour le calcul de la diffraction d'une onde acoustique par une surface rigide," *Mathematical Methods in the Applied Sciences*, Vol. 8, No. 1, 1986, pp. 598–608.

[25]Burton, A. and Miller, G., "The application of integral equation methods to the numerical solution of some exterior boundary-value problems," *Proceedings of the Royal Society of London. A. Mathematical and Physical Sciences*, Vol. 323, No. 1553, 1971, pp. 201–210.

[26]Chappell, D. and Harris, P., "On the choice of coupling parameter in the time domain Burton–Miller formulation," *The Quarterly Journal of Mechanics & Applied Mathematics*, Vol. 62, No. 4, 2009, pp. 431–450.

[27]Yu, K. H., Kadarman, A. H., and Djojodihardjo, H., "Development and implementation of some BEM variants—A critical review," *Engineering Analysis with Boundary Elements*, Vol. 34, No. 10, 2010, pp. 884–899.

[28]Frostig, R., Johnson, M. J., and Leary, C., "Compiling machine learning programs via high-level tracing," *Systems for Machine Learning*, Vol. 4, No. 9, 2018.

[29]Blondel, M., Berthet, Q., Cuturi, M., Frostig, R., Hoyer, S., Llinares-López, F., Pedregosa, F., and Vert, J.-P., "Efficient and modular implicit differentiation," *Advances in neural information processing systems*, Vol. 35, 2022, pp. 5230–5242.

[30]Bowman, J. J., Senior, T. B., and Uslenghi, P. L., "Electromagnetic and acoustic scattering by simple shapes (Revised edition)," *New York*, 1987.